Scalable Reflective Plasmonic Structural Colors from Nanoparticles and Cavity Resonances – the Cyan-Magenta-Yellow Approach

ADVANCED OPTICAL MATERIALS
www.advopticalmat.de

Scalable Reflective Plasmonic Structural Colors from Nanoparticles and Cavity Resonances – the Cyan-Magenta-Yellow Approach

Jolie C. Blake, Stefano Rossi, Magnus P. Jonsson, and Andreas Dahlin**

Plasmonic metasurfaces for color generation are emerging as important components for next generation display devices. Fabricating bright plasmonic colors economically and via easily scalable methods, however, remains difficult. Here, the authors demonstrate an efficient and scalable strategy based on colloidal lithography to fabricate silver-based reflective metal–insulator–nanodisk plasmonic cavities that provide a cyan-magenta-yellow (CMY) color palette with high relative luminance. With the same basic structure, they exploit different mechanisms to efficiently produce a complete subtractive color palette. Finite-difference time-domain simulations reveal that these mechanisms include gap surface plasmon modes for thin insulators and hybridized modes between disk plasmons and Fabry–Pérot modes for thicker systems. To produce yellow hues, they take advantage of higher-energy gap surface plasmon modes to allow resonance dips in the blue spectral region for comparably large nanodisks, thereby circumventing difficult fabrication of nanodisks less than 80 nm. It is anticipated that incorporation of these strategies can reduce fabrication constraints, produce bright saturated colors, and expedite large-scale production.

1. Introduction

Metasurfaces have opened new routes for exploring alternatives to conventional pigment or dye-based coloration. The appeal of metasurfaces for structural colors stems from the manifold advantages they have over pigmentary methods. Traditional modes of color generation are chemically unstable at high temperatures, subject to bleaching if exposed to intense UV illumination, difficult to dispose of or recycle due to toxic composition, and unsuitable for miniaturized imaging and display devices.[1] In favorable contrast to these methods, metasurfaces have shown to be more robust to chemical deterioration,[2] can deliver high spatial resolution[3] and are potentially more economical and sustainable while still rendering colors that are vibrant and aesthetically gratifying.[4,5]

As synthetic composites, metasurfaces can assume a variety of configurations and consist of different combinations of materials such as metals and dielectrics in either nanostructured or thin film forms. The components are specifically selected to create a surface with desired properties. Metasurfaces can produce either transmissive or reflective colors, generated by dielectric components,[6] plasmonic metals,[7,8] or combinations of both.[9] In plasmonic metallic nanoparticles, resonant behavior occurs when incident photons excite surface plasmons at the metal–dielectric interface. This interaction leads to selective filtering of transmitted and reflected light. The strong field enhancement and subwavelength confinement characteristic of this phenomenon have led to the realization of several advancements in structural colors,[1,5] in particular with respect to the delicate balance between chromaticity and absolute reflectance across the visible.[10]

In constructing metasurfaces for color generation, one prominently used geometry is the metal–insulator–metal (MIM) arrangement. In this tri-layer structure, thin metallic films make up the top and bottom layer, while a dielectric (insulator) material fills the central gap.[11–14] A simple approach is to only use multilayered thin films (1D systems) and Fabry–Pérot (FP) effects.[15] However, including lateral sub-wavelength patterns in the MIM system opens up many more possibilities to tune the structural colors by additional resonances determined by the shape and size of the individual elements. MIM structures with nanostructures on top and a very thin dielectric spacer (tens of nanometers) can exhibit so called gap surface plasmons (GSP).[16,17] The principle behind this physical phenomenon involves strong nearfield coupling between plasmon

J. C. Blake, A. Dahlin
Department of Chemistry and Chemical Engineering
Division of Applied Chemistry
Chalmers University of Technology
Göteborg 41296, Sweden
E-mail: adahlin@chalmers.se

S. Rossi, M. P. Jonsson
Department of Science and Technology
Laboratory of Organic Electronics
Linköping University
Norrköping 60174, Sweden
E-mail: magnus.jonsson@liu.se

The ORCID identification number(s) for the author(s) of this article can be found under https://doi.org/10.1002/adom.202200471.

DOI: 10.1002/adom.202200471

modes of the nanostructure and the bottom metallic layer,[18] which leads to strong electric field confinement and the generation of a magnetic dipole in the gap or spacer layer. If the insulator thickness is increased, however, nearfield coupling weakens and the GSP mode transitions to a localized surface plasmon (LSP) of the nanostructure and Fabry–Pérot (FP) type resonances of the cavity formed between the metal layers.[19] In turn, the LSP and FP resonances in this thick insulator limit may also hybridize. This is characterized by a splitting of the resonance modes and was, for example, reported to enhance the reflection capability of the mode.[20] MIM structured plasmonic metasurfaces are well suited for the sub-diffraction limit pixel design and high spatial resolution. Multiple studies have proven the efficacy and tunability of such platforms for producing high performance colors.[4,9,21] The color can be tuned by changing the geometry or periodicity of the nanostructures, or by varying the dielectric layer thickness.

Studies of plasmonic colors based on MIM structures are frequently assessed on their chromaticity, while brightness (absolute reflectance/transmittance) is often not addressed as much. This means that many structural colors may not exhibit good visibility in ambient light despite their high chromaticity. Few studies actively addressed strategies to improve brightness within a gamut or to achieve balance between chromaticity and brightness appropriate for an application.[21–23] In this context, a major appeal of a subtractive color palette is the potential for producing brighter colors than that of a red, green, and blue (RGB) gamut. The subtractive colors cyan, magenta, and yellow (CMY) inherently reflect more of the visible spectrum. Indeed, ink printers use CMY rather than RGB to enhance image brightness. However, although nanostructures, that is, not simply planar film systems, exhibiting CMY colors have been investigated in transmission mode,[24–26] there are few reports of MIM nanostructured surfaces that utilize the CMY gamut for full color in reflection mode.[27–30] In particular, previous work was restricted to production using electron or ion beams, which is not compatible with large-area fabrication. Here, we present a systematic study of large-area reflective CMY colors by employing the hole-mask colloidal lithography (HCL) method to fabricate nanodisks (NDs) as the top layer of MIM reflective plasmonic metasurfaces. We use silver (Ag) as the bottom mirror, alumina (Al_2O_3) as the insulator spacer layer, and Ag nanodisks as the top layer. The strongly scattering Ag ND layer effectively acts as a narrow-bandwidth mirror that upon mode matching can enable FP resonances for large insulator thicknesses. For low insulator thicknesses, the system instead supports GSPs. Furthermore, we demonstrate that changing the dielectric thickness alone provides a simplistic route to expand the color gamut and to tune brightness. Reflective CMY color performance is evaluated in terms of chromaticity and brightness for various combinations of disk sizes and spacer thicknesses, including comparison with the RGB approach. To access resonances on the short wavelength (blue) end of the visible spectrum we also investigated high-energy GSP modes, which overcome the requirement of fabricating very small nanodisks. This approach increases the tolerance to critical-dimension control and facilitates future industrial upscaling and mass production. Lastly, numerical simulations provide further insight into the underlying mechanisms involved in the formation of the specific resonances.

2. Results and Discussion

2.1. Silver Nanodisk Metasurface Structure and Fabrication

Figure 1 describes the preparation of the metasurfaces used in this study. The Ag based metasurface follows a MIM configuration where Ag NDs, exhibiting short-range order, lay on top of continuous thin film layers of Al_2O_3 and Ag. The non-periodic distribution of the NDs arises from the colloidal self-assembly approach of HCL[31] and has the advantage of producing polarization insensitive color-filtering at normal incidence.[25] In the layer profile (Figure 1b), the ND diameter (d), the ND height (h), and the thickness of the Al_2O_3 insulator layer (t) represent the parameters that were varied for producing the subtractive color gamut. Figure 1c illustrates deconstructed and complete views of the metasurface. Figure 1d shows a photograph of a sample where the different layers are separated into regions (1)–(3). Reflection and transmission spectra of these regions are shown in Figure 1e.

In the absence of long-range order and with sufficiently large inter-disk space (>100 nm), the color-filtering feature of the ND array (1) (without the Al_2O_3 and mirror) occurs via uncoupled LSPs, as tunable by d and h.[32] Upon addition of the insulator and bottom mirror (3), transmission is eliminated and the insulator thickness t provides an additional parameter for tailoring the spectral resonance position and quality. The structure without NDs which only has the bottom mirror and insulator layer (2) provides broadband high reflectance in the whole visible region. We noted only a very weak effect of sample aging, that is, the structural colors were stable over 260 days (Figure S1, Supporting Information), suggesting that oxidative degradation of silver is not particularly severe. For perfect stability, protective coatings can be used.[33,34]

2.2. Demonstration of CMY Reflective Colors

The fine tuning of the geometrical parameters (d, h, and t) was guided by finite-difference time-domain (FDTD) simulations, as discussed later, to effectively optimize the reflection spectra of the subtractive color palette. **Figure 2** presents scanning electron microscope (SEM) images and photographs of example samples with clear cyan, magenta, and yellow reflective colors. The experimentally determined diameter of the Ag NDs and the thickness of the Al_2O_3 layer for cyan, magenta, and yellow were 120 and 307 nm, 89 and 227 nm, and 143 and 31 nm respectively. We found the performance of all the metasurfaces to be good at ND heights of ≈30 nm. Note that performance here refers mostly to chromaticity (color purity) but also to brightness. The resonance widths are generally very suitable for eliminating one of the primary colors fully (i.e. they are comparable to one third of the width of the visible interval) while maintaining high reflectance in the remaining part of the visible. In other words, a good balance between chromaticity and brightness can be reached.[10] For comparison, certain dielectric structures could likely cause much sharper resonant features in the reflectance spectrum, but this would eliminate so much of the incident light that the overall visibility would be strongly reduced. This can be properly quantified by the relative

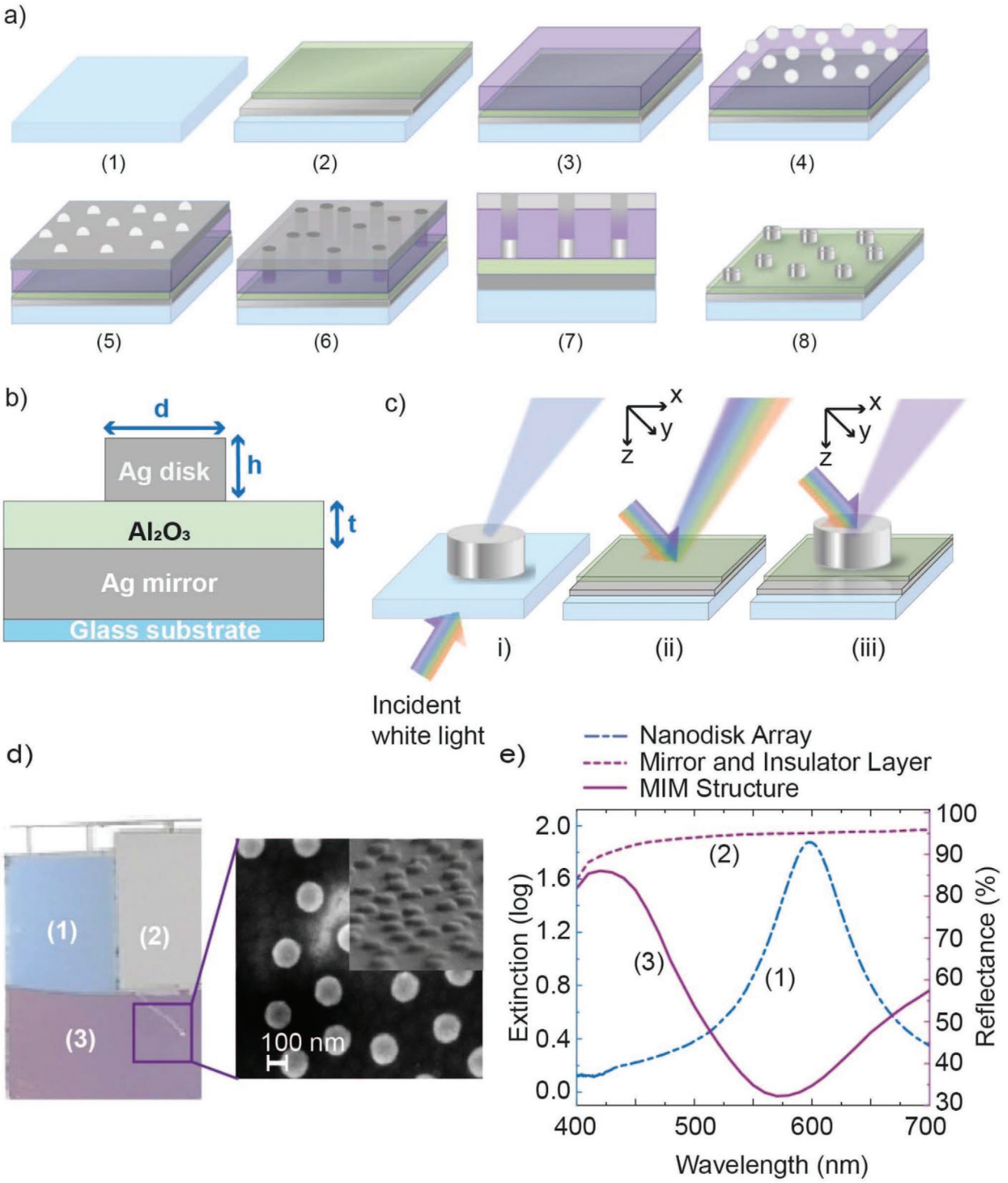

Figure 1. a) Parallelized fabrication steps for producing the metasurfaces by hole-mask colloidal lithography (details given in the Experimental Section). b) Layer profile representation of the plasmonic metasurface, showing a single Ag nanodisk, where *d* represents nanodisk diameter, *h* is the nanodisk height, and *t* is the thickness of the insulator layer (Al_2O_3). c) Schematic of i) Ag nanodisk, ii) Al_2O_3 and Ag thin films, and iii) the complete nanodisk and thin film metasurface, all on a glass substrate. d) Photograph of a fabricated sample, positioned on white background, where the different layers of the metasurface have been isolated into regions (1)–(3) illustrated in (a), and SEM image of an Ag nanodisk array (region 3). The inset shows a tilted (10°) view of the nanodisk surface mounted vertically to obtain a cross section view. e) Extinction spectra of area 1 (only NDs) and reflection spectra for area 2 (only thin films) and 3 (the complete structure).

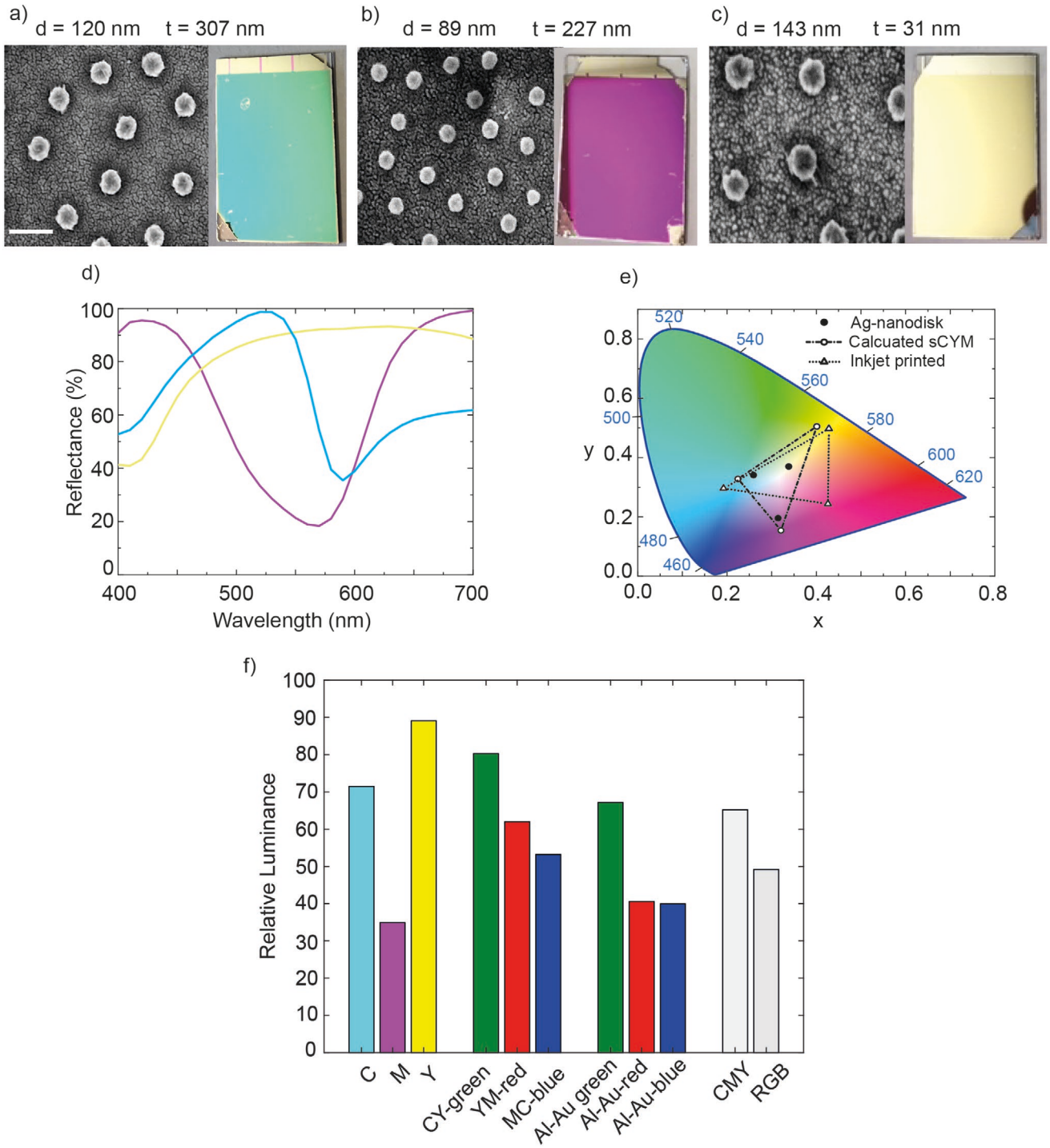

Figure 2. a) SEM image of the top view of a cyan metasurface (scale bar 200 nm) and photograph of the sample (d = 120 nm, h = 30 nm, and t = 307 nm). b) Same for magenta (d = 89 nm, h = 30 nm, and t = 227 nm). c) Same for yellow (d = 143 nm, h = 30 nm, and t = 31 nm). d) Reflectance spectra of the samples. e) CIE 1931 diagram showing the corresponding chromaticity coordinates of the optimized reflected colors compared with a calculated sCMY color gamut and measurements on laser-jet printed CMY colors. f) Bar chart of average relative luminance[10] of the CMY color palette produced by Ag nanodisk structures in this study and the relative luminance of the RGB color palette generated from the CMY colors, which is then compared with previously published Al–Au nanohole metasurfaces.[35] The white values are also compared (averages of Al–Au RGB and Ag CMY).

luminance parameter Y which takes into account the human eye sensitivity for different wavelengths over the whole visible range.[10]

The HCL method yields a distribution of ND diameters due to the intrinsic size distribution of the colloidal polystyrene beads. The absence of long-range order is readily apparent in

all the samples, but the existence of some short-range order, a pseudo periodicity, should also be noted.[31] This short-range order is determined by the electrostatic repulsion between particles. The inherent size-specific dispersion of particles on the surface sufficiently spaces the fabricated nanodisks, hence effectively minimizing near field coupling. A tilted view (Figure 1c), reveals the NDs to have rounded edges and slightly slanted side walls due to the continuous closure of holes in the hole-mask with prolonged deposition.[31]

Figure 2d presents reflectance spectra of the same samples as in panels a–c. Resonant reflection minima were observed at wavelengths 590, 550, and 420 nm for the cyan, magenta, and yellow samples, respectively. The metasurface reflecting magenta color exhibited the deepest reflection minimum at 18%, followed by cyan (35%) and then yellow (41%). The magenta sample also showed the most symmetric reflectance spectrum, with reflectance reaching values greater than 95% in both the red-shifted and blue-shifted off-resonance regions. Notably, the relative luminance is still the lowest because the human eye sensitivity is maximized in the middle of the visible, where the magenta samples absorb light. The blue-shifted off-resonance reflectance of cyan surpassed 98%, while the red-shifted off-resonance band was 61%. For the reflection spectrum of the yellow sample, the reflectance was maximized at 88% in the off-resonance red-shifted region. The color purity and performance were also assessed by plotting the chromaticity coordinates (Figure 2e) computed from the measured reflection spectra of the optimized colors on the standard International Commission on Illumination (CIE 1931 with D65 illuminant) chromaticity diagram. The magenta sample is furthest away from the central white spot (D65 point) followed by the cyan and yellow samples. By tuning the parameters d, h, and t it was possible to extend the gamut even further, but with the risk of lowering the overall reflectance (Figure S2, Supporting Information). As another gauge of color performance, the colors produced by the fabricated metasurfaces are compared to a calculated standard CMY (sCMY) color space, derived from the sRGB standard default color space (see Supporting Information for derivation), as well as printed CMY colors on white paper using a laser printer. The gamut produced by the metasurfaces was ≈27% in area of the calculated standard CMY (sCMY) gamut, with the chromaticity of the magenta and cyan samples being nearer to the standard magenta and cyan chromaticity values than the yellow sample. Notably, the color gamut of the laser-jet printed CMY samples does not encompass the full gamut of the fabricated samples, in particular for hues of magenta. The reflectance ivity of the samples depended on angle of incidence, but major changes were only observed at very high angles (45° or more, Figure S3, Supporting Information).

To quantify the improvement in relative luminance (Y) for the CMY approach, we compare the CMY samples with our previously published gold–aluminum (Au–Al) nanohole reflective MIM metasurfaces that produce a red-green-blue (RBG) palette (Figure 2f).[35] The average relative luminance of the CMY samples is clearly much higher than that of the RGB color palette. We also evaluated RGB colors generated by linear combinations of CMY with that of ordinary RGB, that is, $R = (Y + M)/2$, $G = (C + Y)/2$, and $B = (M + C)/2$. In other words, the "subtractive" color scheme is used in an "additive" manner. This leads to a reduction in chromaticity due to increased white "background" reflectance but again the relative luminance is strongly improved compared to the ordinary RGB (Figure 2f).

The parameter that most strongly influences the cavity resonances in the MIM system is the thickness of the insulator. **Figure 3** shows reflection spectra along with secondary and tertiary occurrences of similar colors for different Al_2O_3 thicknesses, while keeping nanodisk sizes the same for each of the three colors. The corresponding chromaticity coordinates for the different occurrences are also shown. For cyan, the sample with the thinnest insulator layer, 123 nm Al_2O_3, had the shallowest resonance reflection dip (>60% at 600 nm) compared to the other thicknesses. At a 448 nm thickness of Al_2O_3, three minima appear in the reflection spectrum (430, 570, and 660 nm). The main resonance dip has split into two, which is indicative of hybridization between disk plasmons and the cavity.[20] Despite the occurrence of multiple reflection dips, the chromaticity coordinates move away from the D65 point (more saturated color), which is due to the increasing magnitude of the reflection minima of the thickest sample. Similar to cyan, the resonant reflection dip for magenta also deepens for the samples with higher Al_2O_3 thickness. No additional reflection dips appear, but the existing dip progressively narrows while maintaining the same depth for the two thickest samples. As shown in the chromaticity diagram (Figure 3b) this dip narrowing leads to a small decrease in color saturation. It should be noted that while a narrow transmission band translates into high color purity (of the transmitted light), this is not the case for a narrow dip in the spectrum of reflected light.

For the yellow-colored samples (Figure 3c) we varied both the Al_2O_3 layer thickness and the nanodisk diameter and achieved similar hues. As discussed further below, this is because the thin sample (t = 31 nm) utilized large disks to excite a high-energy GSP mode. The reflection dip of the sample with small disks and a thick spacer layer (solid line) is deeper (45%) than for the sample with larger disks and thin spacer layer (60%), while the off-resonance reflection is lower. On the chromaticity plot these differences result in marginally increased color performance for the yellow sample with smaller disks. Neither of the yellow reflectance spectra show reflection dips with depths comparable to those as for the magenta or cyan samples.

2.3. Mechanisms for Selective Color Filtering

We performed FDTD simulations to interpret the experimental results and guide the optimization of color quality. This method can predict the position of the dips and the reflectance values, giving insights on, for example, hybridization between the LSPs and the FP cavity. We simulated the experimental nanodisk arrays using periodically arranged Ag nanodisks and a square lattice periodicity to match the nanodisk surface density experimentally determined by image analysis for each colloid size.

Figure 4 shows a comparison between experimental results and simulations for selected CMY samples, including electric nearfield profiles at the reflectance dip positions. For magenta (Figure 4a) the simulation shows a main dip at 496 nm and a shoulder at higher wavelengths, indicating hybridization between the LSP and the FP mode. The 227 nm spacer height

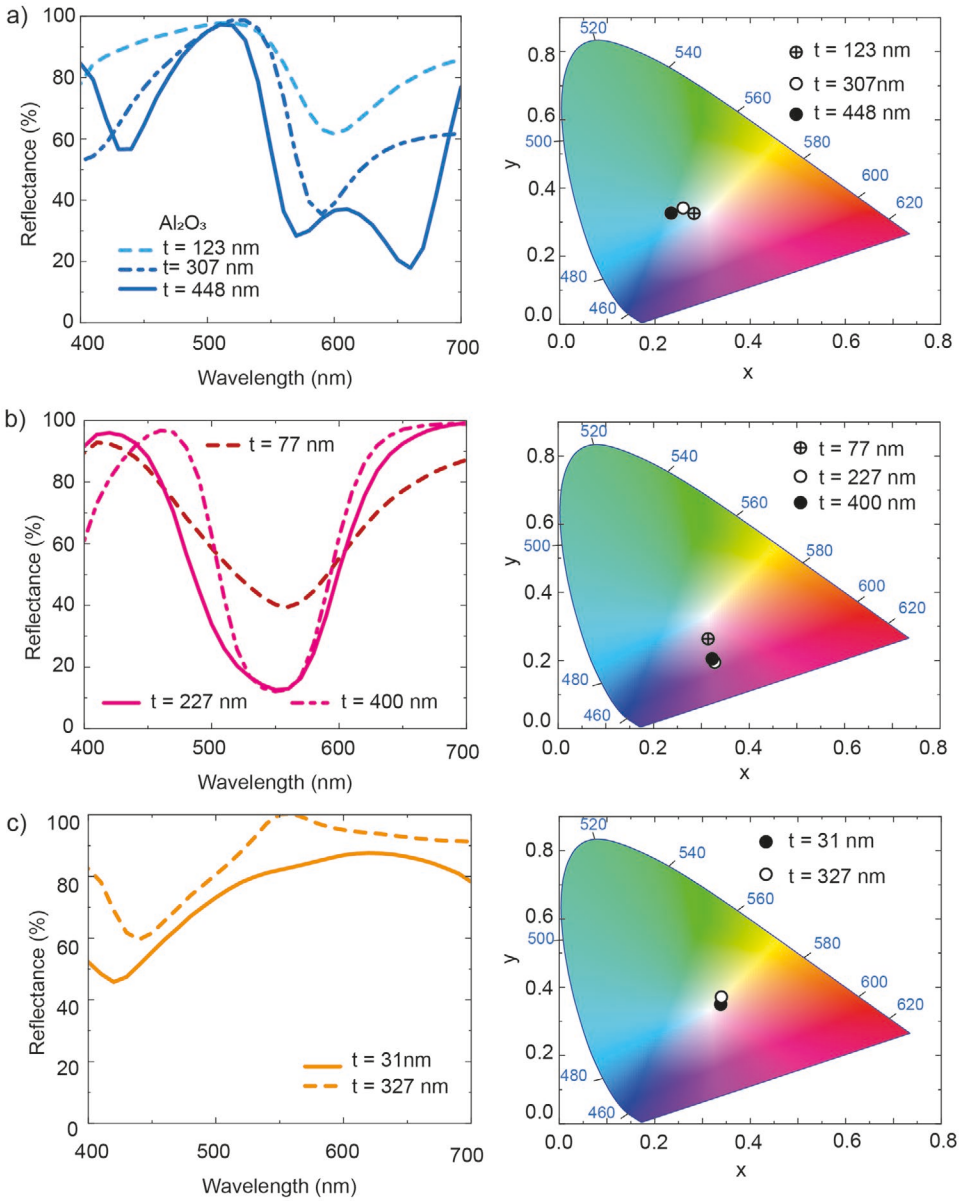

Figure 3. a) Reflection spectra at different layer thicknesses of Al_2O_3 for cyan (d = 120 nm and h = 30 nm). b) Similar tuning of Al_2O_3 thickness for magenta samples (d = 89 nm and h = 30 nm). c) Reflection spectra for two yellow samples with different thicknesses of Al_2O_3 and different nanodisk diameters (d = 89 nm and t = 327 nm, d = 143 nm and t = 31 nm). In all cases, changes in chromaticity are also illustrated.

of this sample corresponds to a condition for which the lower energy dip has a decreased absorption efficiency compared to the higher energy hybridized mode (see the corresponding thickness range in Figure S4a, Supporting Information), hence the presence of a shoulder rather than two clear dips. Besides the evident spacer thickness dependent mode splitting for thicknesses from ≈200 to ≈350 nm (Figure S4a, Supporting Information), the FP contribution to the optical response is also clear by the presence of a node inside the spacer (second order FP resonance). However, only a single broad dip is found in the experimental results. We attribute this effect primarily to the relatively large size distribution of the colloids and other anomalies associated with the lithography step during fabrication (Figure S5, Supporting Information). Nonetheless, the experimental peak falls in between the simulated hybridized peaks and can reproduce magenta with good chromaticity as illustrated in Figure 3b.

For cyan we selected two samples with spacer thicknesses of 307 (Figure 4b) and 448 nm (Figure 4c), since they show different phenomena. In both cases, the simulations show sharp dips in the blue region due to diffraction effects, as is clear from the dependence of the position of those dips with the periodicity (Figures S6b,c, Supporting Information), which cannot be seen in the experimental samples due to the lack of periodicity. This illustrates that the short-range ordered pattern, which gives relatively weak diffraction effects,[36] is actually

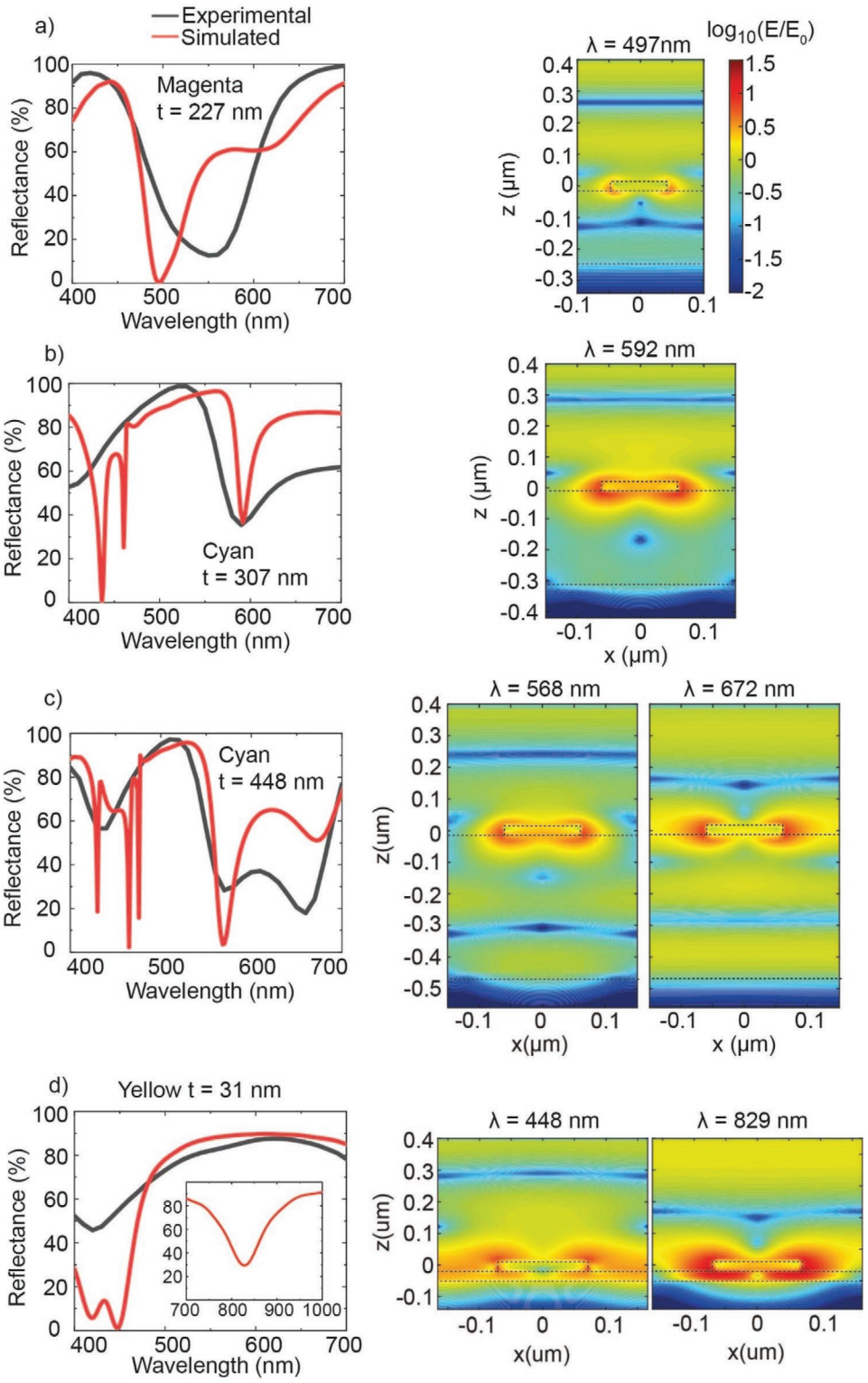

Figure 4. a) Simulated (red line) and experimental (black line) results for a magenta sample (d = 89 nm, periodicity 204 nm). The electric near-field is visualized at the (simulated) reflectance minimum. b) Same for a cyan sample (d = 120 nm, periodicity 302 nm). The near-field is visualized at one of the reflection minima. c) Same for another cyan sample. The near-field is visualized at two different reflectance minima. d) Same for a yellow sample (d = 143 nm, periodicity 333 nm). Here one near-field plot is for a minimum which appears outside of the visible region (inset in spectra). All the near-field distributions have the same color scale. The black dotted lines on the field profiles highlight the geometrical structure.

beneficial compared to long-range ordering (as in the simulations) because very sharp dips do not improve chromaticity and diffraction causes strong angular dependence. The sample with the thinner spacer layer shows a single peak (Figure 4b), whose position and reflectance agrees well with the simulations. The corresponding near-field distribution shows a LSP-dominated resonance, with a highly localized electric field around the nanodisk and a quite uniform field profile inside the spacer. This indicates that in this case there is no important FP contribution to the optical response. In turn, this could be related to the wavelength-dependent scattering of the NDs, which makes their ability to act as the top FP mirror wavelength-dependent. We also note that this spacer thickness is outside the hybridization condition (Figure S4b, Supporting Information). By contrast, the cyan sample with the thicker layer has a clear LSP–FP hybridization, with two dips appearing above 500 nm in both the experimental and simulated results (Figure 4c). For both dips, the near field distribution reveals two nodes inside the spacer layer, indicating that the coupling hybridization involves the third order FP resonance. Simulations for different spacer thicknesses indeed confirm that 448 nm thickness is within a thickness range with clear reflectance dip splitting (Figure S4b, Supporting Information). Discrepancies between the experimental and simulated results are likely due to uncertainties in experimental parameters, such as distribution of ND diameters and exact spacer thickness, on which the hybridized dips are highly dependent.

For yellow, we chose to focus on the configuration with a thin spacer layer (31 nm) because it is different from the other configurations as it provides a typical GSP resonance character based on coupling between the nanodisk dipolar mode and the mirror (Figure 4d). This causes a bonding peak outside the visible at 829 nm (see inset of Figure 4d and near-field plot) and an anti-bonding peak[20] at 448 nm. It is this higher energy antibonding resonance that we exploited to make yellow, avoiding the problem of low absorbance efficiency of the bonding gap plasmon peak for the small nanodisk diameters that would be necessary to absorb in the blue (see also Figure S7, Supporting Information). The simulation shows a further splitting of the anti-bonding gap plasmon peak due to hybridization with surface lattice resonance (see the appearance of a splitting of the dip for larger periods in Figure S6d, Supporting Information), which is not present for lower period and, as expected, cannot be seen in the non-periodic experimental samples. While we experimentally observed a slightly better chromaticity in the thicker (non-GSP) sample (Figure 3c), this does not agree with simulations, which suggested that the GSP-based sample should guarantee a much better yellow chromaticity (see Figure S7b, Supporting Information). This is mainly due to the lower experimental absorption dip in the blue region. In addition, the t = 327 nm and d = 89 nm sample should present a clear splitting of the dip (see Figure S6a, Supporting Information, in the 300–400 nm thickness range), which would significantly change the chromaticity (upon the addition of an absorption dip in the green region along with the blue one) and this is not seen in the experimental sample. Experimental factors such as the polydispersity of the polystyrene beads size within batches, the formation of metal oxide layer on the NDs upon exposure to ambient conditions, the absence of periodic ND distribution, and the fabricated shape of the NDs may cause the experimental parameters to deviate from that predicted by the simulated results. The quality of the polystyrene beads is very important for fabricating reproducible samples that can be predicted by simulations. Therefore, upon a better experimental optimization, it should be feasible to significantly increase the chromaticity for yellow samples.

We also investigated the absorption cross section of a single ND in a cavity in a scattering model with perfectly matched layers (Figure S8, Supporting Information). This model showed a clear spacer thickness dependent magnitude of the absorption cross section, with a strong absorption only at certain thickness ranges. We attribute this to the favorable coupling of the LSP with the reflected standing wave, as confirmed by the presence of a second order absorption maximum for a nanodisk with 90 nm diameter (Figure S8, Supporting Information) at about a doubled Al_2O_3 thickness but with no significant variation of the resonant wavelength. The coupling with the maximum of the standing wave significantly enhances the absorption compared to the ND with no mirror (Figure S9, Supporting Information).

3. Conclusion

In this work we have demonstrated a silver based MIM nanoplasmonic metasurface for subtractive CMY color generation, fabricated using a scalable large-area colloidal hole-mask lithography technique. This is the first demonstration of large-area subtractive structural colors in the reflection configuration utilizing multiple resonant phenomena in laterally nanostructured MIM metasurfaces. We tailored the resonance positions by adjusting ND dimensions as well as the dielectric spacer thickness, to obtain a wide subtractive color palette with an increased relative luminance compared to previously investigated RGB plasmonic metasurfaces. The combined effect of enhancement of the nanodisk localized plasmonic resonance inside the optical cavity and the hybridization with the Fabry–Pérot interference made it possible to reproduce the CMY primary colors using a combination of different nanodisk diameters and spacer thicknesses. In contrast to single nanodisks on a dielectric, the integration on an optical MIM cavity allows for efficient plasmonic absorption, along with an additional tunability of the resonance with the spacer thickness control. Additionally, keeping the same sample geometry, we exploited higher energy antibonding resonances in hybridized optical nanocavities with thin spacers to create yellow hues. The use of the higher energy resonance, instead of the lower energy bonding mode, solves the problem of achieving efficient absorption in the blue with gap plasmons, without the need for less absorptive low diameter nanodisks.

We believe that this work provides a simple alternative approach toward the fabrication of metasurfaces with a subtractive color palette and a feasible route to industrial up-scaling. One challenge in such applications is to realize differently colored structures next to each other on the microscale, for color mixing and image creation. This could potentially be achieved with recently developed advanced laser "printing" techniques, which provide features such as femtosecond pulsing and dual beams etc.[37] Such methods have already been implemented for

steganography and hidden images.[38,39] Although laser writing is serial in nature, it is quite fast and the exposure pattern is easily adjusted. Alternatively, a fully parallel method would be UV-light based patterning, which is also compatible with electrochromic materials for subsequent color image tuning.[40]

4. Experimental Section

Nanofabrication of Silver Metasurfaces: Glass substrates (18 mm × 24 mm) were cleaned by sonication in acetone followed by isopropyl alcohol (IPA) and then dried using nitrogen gas. Thin film mirror layers of silver (150 nm) and dielectric layers of Al_2O_3 were deposited onto the cleaned glass substrates using an automated electron beam system Lesker PVD 225. An adhesion layer of 5 nm Ti was deposited below the mirror layer. A sacrificial layer of poly (methyl methacrylate) (950 MMA A4) was spin coated onto the thin film layers using a photo resist spinner (Suss MicroTec LabSpin6) and heat cured for 10 min at 180 °C in a furnace. The coated substrates were then subjected to a 5 s oxygen plasma etch (PlasmaTherm Reactive Ion Etcher RIE) to make the surfaces more hydrophilic. Colloidal lithography was performed using polystyrene bead colloids ranging in size from 99 ± 4 to 147 ± 7 nm (Microparticles GmbH). A thin film of Cr (10 nm) was deposited onto the dispersed colloids and the colloid beads taped stripped away leaving a nanohole mask. Reactive ion etching of O_2 (5–6 min) was applied to the hole mask to deepen the cavities for deposition. Ag was deposited onto the surface after a 1 nm adhesion layer of Ti. Acetone followed by IPA was used to lift-off the spin coated layer to reveal metallic disks on a mirrored surface.

Ink-Jet Printed Colors: The printed colors of cyan, magenta, and yellow were produced using the drawing program Microsoft Paint. The colors were selected based on the 8-bit sRGB normalized color scale where colors are defined using three values ranging from 0–255, for hue, saturation, and luminance. For cyan (R: 0, G: 255, B: 255), the hue was 120, the saturation 240, and the luminance 120. For magenta (R: 255, G: 0, B: 255) the hue was 200, the saturation 240, and the luminance 120. The colors were printed on standard white A4 copy paper using a Kyocera 5052ci laser printer.

SEM and Optical Characterization: Reflectance spectra for fabricated samples as well as ink jet printed samples were measured using a Konika Minolta spectrophotometer (CM-700d). The instrument also automatically calculates International Commission on Illumination (CIE) coordinates for the assigned 2° standard observer as well as relative luminance (*Y*). The SEM micrographs and measurements of the ND were performed using a Zeiss Supra VP 60 SEM at 3 keV. High angle reflectance measurements were taken with J. A. Woolam M2000 spectroscopic ellipsometer. Ellipsometry was also used to determine the refractive index of the Al_2O_3 thin film layer.

Numerical Calculations: Numerical simulations for the spectra and field profiles were done by FDTD using the commercial software Lumerical FDTD solution. The refractive index of Al_2O_3 was determined experimentally by ellipsometry, while the refractive index of Ag was taken from the Lumerical database and the air was set to $n = 1$. A uniform mesh with conformal 0 refinement was used with $2 \times 2 \times 2$ nm^3 cells in a 3D periodic model. A normal incidence planar wave source with an electric field amplitude of 1 V m^{-1} was set and a square unit cell with the experimental periodicity was used. The periodicity was determined for each colloid size by counting particles on electron microscopy images over a given area. The periodicity is then $[1/\rho]^{1/2}$ with ρ being the number of nanodisks per unit of area. For the single nanodisk scattering model we used a perfectly matched layer boundary condition. The integration of the Poynting vector in the total field region was done including both the ND and the mirror with an integration box inside the source region. For the single NDs the same model was used, changing the mirror material to Al_2O_3 and adding a scattering per unit volume analysis group to determine the scattering cross-section in the scattered field region.

Supporting Information

Supporting Information is available from the Wiley Online Library or from the author.

Acknowledgements

J.C.B. and S.R. contributed equally to this work. This work was financed by the Swedish Foundation for Strategic Research, framework grant EM16-0002.

Conflict of Interest

The authors declare no conflict of interest.

Data Availability Statement

The data that support the findings of this study are available from the corresponding author upon reasonable request.

Keywords

cavities, gap plasmons, lithography, nanostructures, structural colors

Received: February 28, 2022
Revised: April 3, 2022
Published online:

[1] M. W. Song, D. Wang, S. Peana, S. Choudhury, P. Nyga, Z. A. Kudyshev, H. L. Yu, A. Boltasseva, V. M. Shalaev, A. V. Kildishev, *Appl. Phys. Rev.* **2019**, *6*, 041308.
[2] A. S. Roberts, A. Pors, O. Albrektsen, S. I. Bozhevolnyi, *Nano Lett.* **2014**, *14*, 783.
[3] K. Kumar, H. Duan, R. S. Hegde, S. C. W. Koh, J. N. Wei, J. K. W. Yang, *Nat. Nanotechnol.* **2012**, *7*, 557.
[4] M. W. Song, Z. A. Kudyshev, H. L. Yu, A. Boltasseva, V. M. Shalaev, A. V. Kildishev, *Opt. Mater. Express* **2019**, *9*, 779.
[5] A. Kristensen, J. K. W. Yang, S. I. Bozhevolnyi, S. Link, P. Nordlander, N. J. Halas, N. A. Mortensen, *Nat. Rev. Mater.* **2016**, *2*, 16088.
[6] W. Yang, S. Xiao, Q. Song, Y. Liu, Y. Wu, S. Wang, J. Yu, J. Han, D.-P. Tsai, *Nat. Commun.* **2020**, *11*, 1864.
[7] D. Inoue, A. Miura, T. Nomura, H. Fujikawa, K. Sato, N. Ikeda, D. Tsuya, Y. Sugimoto, Y. Koide, *Appl. Phys. Lett.* **2011**, *98*, 093113.
[8] B. Zeng, Y. Gao, F. J. Bartoli, *Sci. Rep.* **2013**, *3*, 2840.
[9] H. Wang, X. Wang, C. Yan, H. Zhao, J. Zhang, C. Santschi, O. J. F. Martin, *ACS Nano* **2017**, *11*, 4419.
[10] M. Gugole, O. Olsson, S. Rossi, M. P. Jonsson, A. Dahlin, *Nano Lett.* **2021**, *21*, 4343.
[11] Z. Li, S. Butun, K. Aydin, *ACS Photonics* **2015**, *2*, 183.
[12] Z. M. Yang, Y. M. Zhou, Y. Q. Chen, Y. S. Wang, P. Dai, Z. G. Zhang, H. G. Duan, *Adv. Opt. Mater.* **2016**, *4*, 1196.
[13] K.-T. Lee, S. Seo, L. J. Guo, *Adv. Opt. Mater.* **2015**, *3*, 347.
[14] N. Andam, S. Refki, S. Hayashi, Z. Sekkat, *Sci. Rep.* **2021**, *11*, 15093.
[15] C.-S. Park, V. R. Shrestha, S.-S. Lee, D.-Y. Choi, *Sci. Rep.* **2016**, *6*, 25496.
[16] F. Ding, Y. Yang, R. A. Deshpande, S. I. Bozhevolnyi, *Nanophotonics* **2018**, *7*, 1129.

[17] R. Deshpande, A. Pors, S. I. Bozhevolnyi, *Opt. Express* **2017**, *25*, 12508.
[18] Q. He, S. Sun, S. Xiao, L. Zhou, *Adv. Opt. Mater.* **2018**, *6*, 1800415.
[19] S. Ma, S. Xiao, L. Zhou, *Phys. Rev. B* **2016**, *93*, 045305.
[20] Z. Sun, Y. Fang, *ACS Appl. Nano Mater.* **2020**, *3*, 10732.
[21] R. Mudachathi, T. Tanaka, *Sci. Rep.* **2017**, *7*, 1199.
[22] R. A. Deshpande, A. S. Roberts, S. I. Bozhevolnyi, *Opt. Mater. Express* **2019**, *9*, 717.
[23] C. U. Hail, G. Schnoering, M. Damak, D. Poulikakos, H. Eghlidi, *ACS Nano* **2020**, *14*, 1783.
[24] X. L. Hu, L. B. Sun, B. Zeng, L. S. Wang, Z. G. Yu, S. A. Bai, S. M. Yang, L. X. Zhao, Q. Li, M. Qiu, R. Z. Tai, H. J. Fecht, J. Z. Jiang, D. X. Zhang, *Appl. Opt.* **2016**, *55*, 148.
[25] M. Ye, L. Sun, X. Hu, B. Shi, B. Zeng, L. Wang, J. Zhao, S. Yang, R. Tai, H.-J. Fecht, J.-Z. Jiang, D.-X. Zhang, *Opt. Lett.* **2015**, *40*, 4979.
[26] V. R. Shrestha, S.-S. Lee, E.-S. Kim, D.-Y. Choi, *Nano Lett.* **2014**, *14*, 6672.
[27] J. Zhao, X. Yu, K. Zhou, X. Yang, Y. Yu, *Nanoscale Res. Lett.* **2019**, *14*, 214.
[28] W. Yue, S. Gao, S. S. Lee, E. S. Kim, D. Y. Choi, *Laser Photonics Rev.* **2017**, *11*, 1600285.
[29] W. Yue, S. Gao, S.-S. Lee, E.-S. Kim, D.-Y. Choi, *Sci. Rep.* **2016**, *6*, 29756.
[30] F. Cheng, J. Gao, T. S. Luk, X. Yang, *Sci. Rep.* **2015**, *5*, 11045.
[31] H. Fredriksson, Y. Alaverdyan, A. Dmitriev, C. Langhammer, D. S. Sutherland, M. Zaech, B. Kasemo, *Adv. Mater.* **2007**, *19*, 4297.
[32] P. Hanarp, M. Kall, D. S. Sutherland, *J. Phys. Chem. B* **2003**, *107*, 5768.
[33] K. Xiong, D. Tordera, G. Emilsson, O. Olsson, U. Linderhed, M. P. Jonsson, A. B. Dahlin, *Nano Lett.* **2017**, *17*, 7033.
[34] S. Elhani, H. Ishitobi, Y. Inouye, A. Ono, S. Hayashi, Z. Sekkat, *Sci. Rep.* **2020**, *10*, 3913.
[35] M. Gugole, O. Olsson, K. Xiong, J. C. Blake, J. Montero Amenedo, I. Bayrak Pehlivan, G. A. Niklasson, A. Dahlin, *ACS Photonics* **2020**, *7*, 1762.
[36] M. Schwind, V. D. Miljkovic, M. Zach, V. Gusak, M. Kall, I. Zoric, P. Johansson, *ACS Nano* **2012**, *6*, 9455.
[37] L. Chen, K. Q. Cao, Y. L. Li, J. K. Liu, S. Zhang, D. H. Feng, Z. R. Sun, T. Q. Jia, *Opto-Electron. Adv.* **2021**, *4*, 200036.
[38] D. Hu, Y. Lu, Y. Cao, Y. Zhang, Y. Xu, W. Li, F. Gao, B. Cai, B.-O. Guan, C.-W. Qiu, X. Li, *ACS Nano* **2018**, *12*, 9233.
[39] Y. Zhang, L. Shi, D. Hu, S. Chen, S. Xie, Y. Lu, Y. Cao, Z. Zhu, L. Jin, B.-O. Guan, S. Rogge, X. Li, *Nanoscale Horiz.* **2019**, *4*, 601.
[40] S. Chen, S. Rossi, R. Shanker, G. Cincotti, S. Gamage, P. Kuhne, V. Stanishev, I. Engquist, M. Berggren, J. Edberg, V. Darakchieva, M. P. Jonsson, *Adv. Mater.* **2021**, *33*, 2102451.